ELSEVIER

Contents lists available at ScienceDirect

Composites Science and Technology

journal homepage: http://www.elsevier.com/locate/compscitech



Comparing non-destructive 3D X-ray computed tomography with destructive optical microscopy for microstructural characterization of fiber reinforced composites



Imad Hanhan a, Ronald Agyei a, Xianghui Xiao b, Michael D. Sangid a, *

- ^a School of Aeronautics and Astronautics, Purdue University, West Lafayette, IN, 47907, USA
- ^b Advanced Photon Source, Argonne National Laboratory, Lemont, IL, 60439, USA

ARTICLE INFO

Keywords: Short-fiber composites Non-destructive testing Optical microscopy

ABSTRACT

Due to their lightweight, relatively high stiffness properties, and formability into complex shapes, discontinuous fiber composites are advantageous for producing small and medium size components. Improved characterization techniques and post-processing methodologies are required for more reliable quantification of the microstructure and defect distributions in these materials, in order to employ model-based approaches to assess their structural integrity. This work compares a non-destructive X-ray approach with a destructive optical microscopy approach for characterizing the microstructural attributes, specifically the fiber volume fraction, porosity volume fraction, fiber orientation distribution, and fiber length distribution of discontinuous glass fibers in a polypropylene matrix. Additionally, a method for destructively determining the ambiguous components of the orientation tensor (related to the sign ambiguity of the out-of-plane angle in a destructive cross-sectional cut of a fiber) over a large surface area is included. It was found that fiber volume fraction and average fiber aspect ratio matched well, while fiber orientation and porosity detection had small but notable differences. The differences in the detection capabilities of each technique are quantified and discussed shedding light on the specific advantages and disadvantages of each approach, and enabling engineers to quantify uncertainty in their microstructural characterization measurements especially as they relate to model based structural integrity activities.

1. Introduction

Short fiber reinforced polymers have gained attention in engineering applications due to their low-cost manufacturability and their ability to be easily fabricated into complex geometries. Since the features of the microstructure largely depend on the injection molding processing parameters, different geometries of injection molded composites can result in vastly different microstructures [1–4]. Often times, qualifying composite materials and predicting their bulk mechanical behavior requires a thorough characterization of their microstructural features including the fiber length and orientation distributions and the gas-phase pores [5–10]. Researchers have therefore developed a number of characterization techniques that can capture the microstructural details of discontinuous fiber composites, most of which are destructive in nature to the part or sample.

Specifically, techniques to measure the fiber orientation

distributions in composites have historically been destructive, and include sectioning and polishing, followed by optical microscopy or scanning electron microscopy (SEM), in order to determine the in-plane and out-of-plane angles of the projected fibers from the surface characterization [11–16]. Techniques to measure the fiber length distributions are also typically destructive and involve heating the specimen to decompose the polymer matrix and down-selecting the fibers using an epoxy plug, in an effort to reduce bias in the measurement based on the potential for fiber breakage due to the release of stored strain energy during the matrix 'burn-off' and fiber separation process. The extracted fibers are then suspended in a liquid such as water or glycerin, poured into a petri dish, and observed in an optical microscope in order to measure the fiber lengths [17–21].

There are some challenges and limitations to these destructive techniques. A widely recognized challenge with sectioning and polishing specimens for fiber orientation analysis is the ambiguity in the 3D fiber

^{*} Corresponding author.

E-mail address: msangid@purdue.edu (M.D. Sangid).

¹ Brookhaven National Lab, Upton, NY, 11973, USA

orientation [12,16,22]. One way to resolve this issue is to determine the ambiguous angle by observing the shadow of each fiber that is exposed during plasma etching of the surface and then viewed in an optical microscope [12]. Another approach is to cut consecutive parallel sections from the composite [23], or successively polish the surface [24], followed by optical microscopy and observation of each fiber. The challenge with these approaches is that they are difficult to implement over a large area for thousands of fibers, which presents issues in characterization over a representative area/volume of the material or capturing gradient behavior in the orientation distribution spatially over a component.

Non-destructive techniques for characterizing the microstructure of composites have also been developed. One technique, known as scanning acoustic microscopy, uses interference fringes that result from echoes reflected by the fibers to conduct nondestructive fiber orientation measurements to depths of approximately 12 µm [22]. However, this technique is limited by the fact that only fibers with out-of-plane angles less than 71.92° can be measured, and measurements deeper than $12 \, \mu m$ require cutting the material [22]. Other techniques for non-destructive evaluation of composites that have become more popular in recent years involve X-ray radiation. Most commonly, high resolution X-ray micro computed tomography (μ-CT) can be used to non-destructively characterize a composite material's microstructural features [25-33]. To understand the quantitative differences in microstructural characterization achieved through non-destructive techniques, researchers have started to explore how fiber orientation distributions achieved through classical destructive optical microscopy differ from those achieved through μ-CT images using a Mean Intercept Length (MIL) technique. A MIL fiber tensor can be constructed to provide a global characterization of the general fiber alignment, but is not capable of capturing each single fiber [34]. Therefore, there remains a need to conduct a one-to-one feature comparison which comprehensively addresses all the microstructural and defect features.

This work addresses porosity and fiber volume fraction, fiber orientation, and fiber length distributions computed using X-ray μ -CT

and optical microscopy as outlined in Fig. 1. This paper will initially discuss the discontinuous fiber composite selected for analysis in this study and next provide detailed methodologies for the characterization methods to determine the porosity volume fraction, fiber volume fraction, fiber orientation, and fiber length distributions, first using X-ray $\mu\text{-CT}$ and then using optical microscopy. Furthermore, the ambiguity in the 3D fiber orientation measurements using destructive optical microscopy was resolved by successive polishing, plasma etching, and post-processed with the introduction of a new automated image processing algorithm, and the details of the algorithm are discussed. Overall, the results of this work provide a practical and useful comparative analysis between non-destructive X-ray $\mu\text{-CT}$ and destructive optical microscopy which comprehensively addresses all aspects of the microstructure.

2. Materials and methods

2.1. Composite material

The material used in this work was a short glass fiber reinforced polypropylene containing 30%, by weight, 10 μm diameter E-glass fibers (corresponding to a fiber volume fraction of 13.7%) manufactured using injection molding by DuPont into a cylindrical rod measuring approximately 1.27 cm (0.5 inch) in diameter and approximately 45.72 cm (1.5 feet) in length, where the flow direction was in the length direction of the rod. The final composite rod was then machined into dog-bone shaped specimens with a gauge section diameter of approximately 2.4 mm. One specimen was selected and imaged using X-ray μ -CT and then sectioned and polished for optical microscopy for a direct comparison of the fiber volume fraction, porosity volume fraction, and fiber orientation distribution, and a second specimen was selected for destructive characterization to provide a statistical comparison of the fiber length distribution.

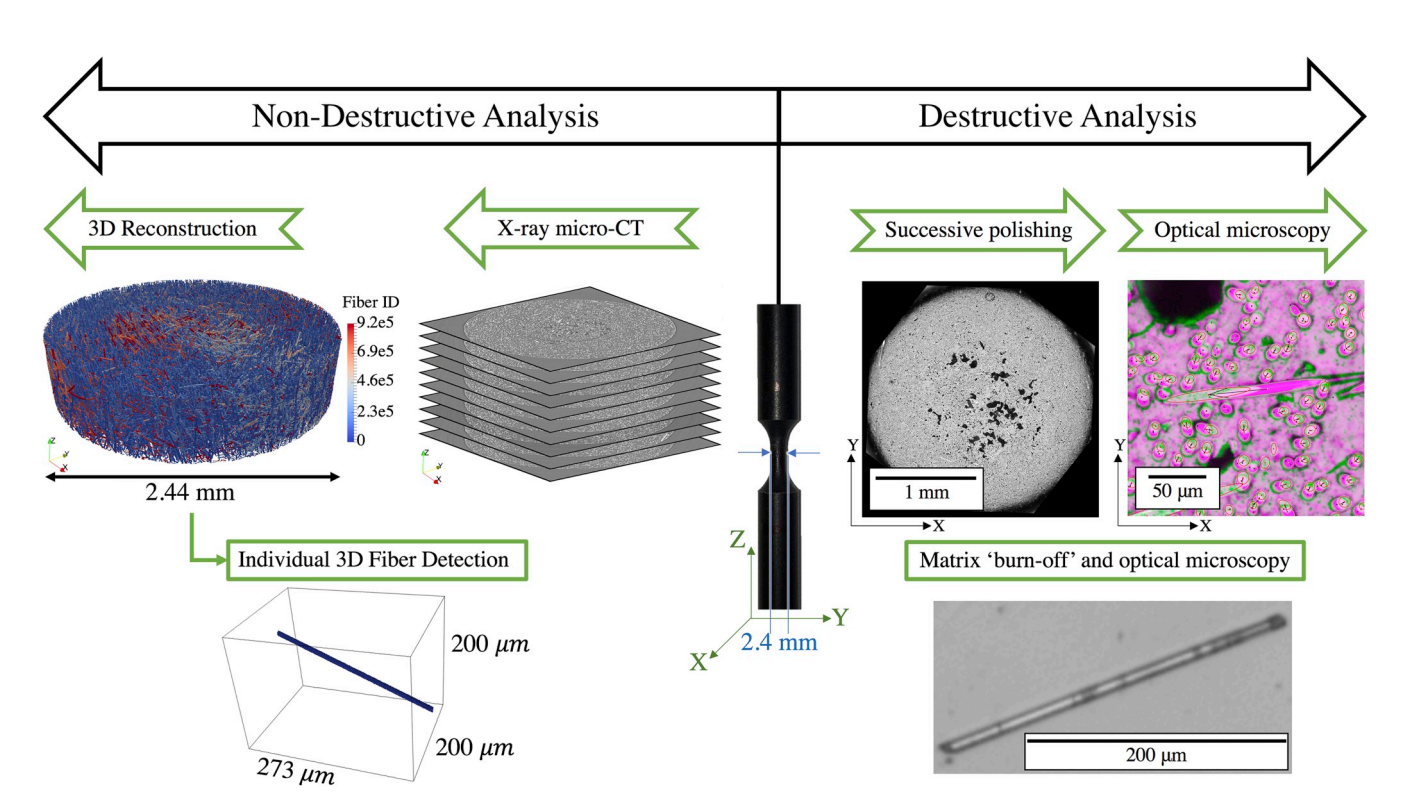


Fig. 1. Comparing non-destructive X-ray μ -CT and typical destructive microscopy techniques for characterizing discontinuous fiber reinforced polymer matrix composites.

2.2. Defining fiber orientation

The orientation of a fiber in 3D space, shown in Fig. 2A, can be characterized by two angles, an in-plane angle ϕ , and an out-of-plane angle θ [35,36]. It is standard to report the orientation of fibers, especially for discontinuous fibers, in the A_{ij} tensor form [35,36], where the components of the p vector are given by

$$p_1 = \sin\theta\cos\phi$$

$$p_2 = \sin\theta\sin\phi$$

$$p_3 = \cos\theta$$
(1)

and where A_{ii} is defined as

 $A_{ii} = p_i p_i$

$$=\begin{bmatrix} \sin^{2}(\theta)\cos^{2}(\phi) & \sin^{2}(\theta)\cos(\phi)\sin(\phi) & \sin(\theta)\cos(\theta)\cos(\phi) \\ \sin^{2}(\theta)\cos(\phi)\sin(\phi) & \sin^{2}(\theta)\sin^{2}(\phi) & \sin(\theta)\cos(\theta)\sin(\phi) \\ \sin(\theta)\cos(\theta)\cos(\phi) & \sin(\theta)\cos(\theta)\sin(\phi) & \cos^{2}(\theta) \end{bmatrix}$$
(2)

In this work, the in-plane angle is defined as $-90^{\circ} \le \phi \le 90^{\circ}$, and the out-of-plane is defined as $-90^{\circ} \le \theta \le 90^{\circ}$. The 2D elliptical cross-section of a fiber, shown in Fig. 2B, contains enough information to determine the magnitude of θ , as well as the magnitude and sign of ϕ , resulting in A_{11} , A_{22} , A_{33} , and A_{12} . Since $\sin(\theta) \ne \sin(-\theta)$, additional 3D information is required to determine the sign of θ in order to resolve A_{13} and A_{23} , which each contain a $\sin(\theta)$ term [15,16,37].

2.3. Non-destructive X-ray μ -CT and feature detection

The selected specimen was studied at Argonne National Laboratory using synchrotron X-ray $\mu\text{-CT}$, which offers significant advantages over lab-scale $\mu\text{-CT}$ analysis, specifically fast data acquisition, on the order of minutes using synchrotron X-rays, compared to hours for lab-based X-ray sources. Prior to imaging, an aluminum fiducial marker was adhered to the center of the specimen's gauge section. An X-ray energy of 25 keV was used to scan the 2.44 mm diameter specimen, which was placed at a specimen to detector distance of 75 mm. Each X-ray projection was acquired with a 100 ms exposure time every 0.12° as the specimen was rotated at 0.5°/s within a range of 180°. The 1500 acquired X-ray projections were reconstructed using TomoPy [38], resulting in 2D images which stack to form a 3D image with dimensions 2560 by 2560 by 1240 pixels and a pixel size of 1.3 μm , as can be seen in the sample images in Fig. 1. From the 3D image stack, the fibers and gas-phase pores can be observed visually but require rigorous image processing and

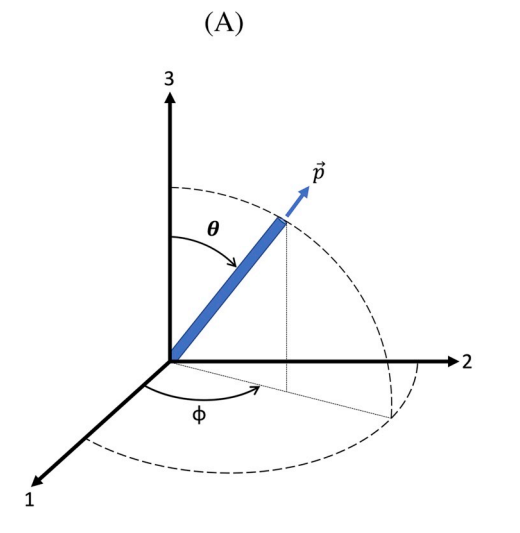
segmentation to extract meaningful, quantifiable data across a large volume. The fiber volume fraction was determined by extracting the high intensity pixels corresponding to fibers. The porosity volume fraction was more complex to determine because large pores contain a combination of low and high intensity pixels in their interior and this gradient causes difficulties in detection and segmentation. To overcome this, a combination of Weka segmentation, a machine learning tool [39], and image processing in MATLAB® (binarization of pixels with intensity less than 17200, followed by erosion and dilation using a spherical structural element with a radius of 2 pixels) was used to create high fidelity 3D porosity reconstructions and compute the porosity volume fraction.

In order to determine fiber orientation and length distributions, a post-processing algorithm developed by Agyei and Sangid was employed, which combines 2D and 3D approaches to provide a complete 3D reconstruction of the fiber microstructure [31]. This allows for quantifying both the 3D fiber orientation distribution and the fiber length distribution in the same analysis. Please see Ref. [31] for additional details which are briefly summarized here for completeness. The algorithm initially processes each 2D image by iteratively enhancing the contrast, segmenting the image, and fitting ellipses around the fiber elliptical cross-sections present in each 2D μ -CT image. Then, this ellipse data is stacked and organized in 3D, and undergoes a number of 3D segmentation steps to determine which ellipses stack to form each individual fiber and correct for errors in the 3D crude fiber architecture that are present due to random intensity fluctuations in the grayscale μ-CT images or imprecise segmentation. All components of the fiber orientation A_{ii} tensor and the fiber length can then be extracted directly for each individual fiber within the composite.

2.4. Destructive optical microscopy

2.4.1. Sectioning, polishing and plasma etching

After acquiring the X-ray μ -CT images of the specimen, it was mounted in acrylic for easy handling, placed in a Buehler EcoMetTM 250/AutoMetTM 250 Pro Grinder/Polisher, and polished to the location of the aluminum fiducial marker. A head rotation speed of 60 rpm was used, and the polishing head was either programmed to rotate in the direction of the polishing pad (>>) or against the direction of the polishing pad (><), with an applied force of 22.24 N (5 lbs) per specimen. The specimen was polished (a) with a 120 grit silicon carbide pad until plane at a speed of 400 rpm (><), (b) with a 320 grit silicon carbide pad for 4 min at a speed of 400 rpm (><), (c) with a 400 grit silicon carbide



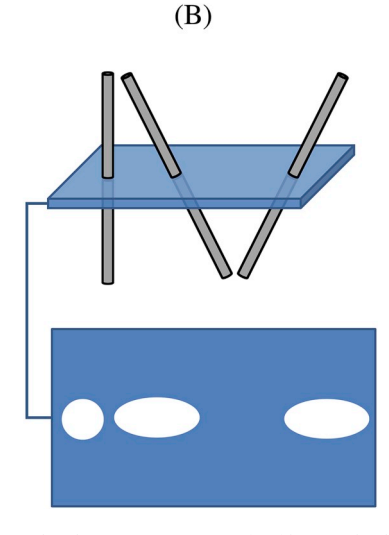


Fig. 2. Schematic (A) showing the in-plane angle ϕ and the out-of-plane angle θ used to describe the 3D orientation of a fiber, and schematic (B) showing the elliptical cross-sections of three fibers, two of which have equal magnitude but opposite signs of θ .

pad for 2 min at speed of 120 rpm (><), (d) with a 600 grit silicon carbide pad for 2 min at a speed of 120 rpm (>>), (e) with 5 μm alumina on a low nap cloth for 90 min at a speed of 120 rpm (>>), (f) with 0.3 μm alumina on a low nap cloth for 60 min at a speed of 120 rpm (>>), and (g) with 0.05 μm alumina on a low nap cloth for 30 min at a speed of 120 rpm (>>). The specimen was sonicated in distilled water after each step, and select images of the surface progression are shown in Fig. 3. It can be observed in the final polished optical image, shown in Fig. 3B, that there is very little contrast between the polypropylene matrix and the glass fibers, but good contrast between the polymer matrix and the porosity. Therefore, the final polished surface was used for porosity detection and for computing the porosity area fraction by extracting the dark pixels of the image.

To enhance the contrast for the purpose of fiber detection, the specimen's surface was plasma etched in a March Jupiter II Etcher with O_2 at a 50 cc flow rate for 1 h at 100 W under a vacuum pressure of 234 mTorr. As can be seen in Fig. 3C, plasma etching dramatically increased the contrast between the matrix and the fibers. Therefore, the plasma etched surface was used for computing the fiber area fraction (by extracting high intensity pixels), as well as the A_{11} , A_{22} , A_{33} , and A_{12} components of the fiber orientation tensor through elliptical fitting of the cross-section of each fiber [15,16,37].

In order to resolve the A_{13} and A_{23} components of the fiber orientation tensor, the polished and etched surface was polished again at the final polish parameter (0.05 µm alumina particle size) for approximately 25 min until the surface resembled Fig. 3B (removing approximately 4.6 µm of material) and then etched again. To summarize, a total of 3 optical images were captured and analyzed: (1) the image of the final polished surface for porosity detection and porosity area fraction computation (referred to as the porosity image), (2) the image of the final polished and etched surface for fiber area fraction and fiber orientation distribution (referred to as the fiber target image), and (3) the image of the successively polished and re-etched surface for resolving the A_{13} and A_{23} fiber orientation components (referred to as the fiber reference image).

These three optical images were acquired using an Olympus BX51M reflected light microscope with an X-Y-Z stage capable of acquiring an automatically stitched image of a large region with automatic focusing and at a user defined magnification. The entire cross-section of the gauge section (2.44 mm in diameter) was optically acquired in a seamless image at 10X with a pixel size of 651 nm.

2.4.2. Destructively determining the sign of the out-of-plane angle

Following the surface preparation, optical imaging, and elliptical fitting of each fiber cross-section, the fiber reference and target images were post-processed to resolve the A_{13} and A_{23} components of the fiber orientation tensor. The in-plane angle ϕ was measured directly from the in-plane elliptical fit of the cross-section of a fiber in the optical image, and the magnitude of the out-of-plane angle $|\theta|$ was determined by the

major and minor axes of the ellipse [15,34]. As can be seen in Fig. 4A, the cross section of a fiber with a positive or negative out-of-plane angle (and the same in-plane angle) will result in the same elliptical cross section, creating an ambiguity in the sign of the out-of-plane angle, θ .

To overcome this ambiguity, the fiber reference and fiber target images were post-processed to uncover the sign of the out-of-plane angle shown in Fig. 4B for thousands of fibers within a given cross section. This was accomplished through a unique automated image processing approach used to match the corresponding cross section of each fiber on the reference and target images. A crucial consideration for this procedure is that the images must be very well aligned. The aluminum foil fiducial marker that was adhered to the surface of the specimen was used to rotate and translate the digital optical micrographs to align them to the same relative position, allowing for any differences in the cross-sectional properties of the fibers to be from the out-of-plane angle, and not due to artificial translations from misaligned images.

Since the rate of removal while polishing was measured and kept constant, the distance between the reference image (shown in Fig. 4C) and the target image (shown as the red ellipse in Fig. 4D) was known and is referred to as h. Through elliptical fitting, the centroid coordinates of each fiber on the reference image, x_i^r and y_i^r , as well as the centroid coordinates of each fiber on the target image, x_k^t and y_k^t were known, where i ranges from 1 to the total number of fiber cross-sections in the reference image, and k ranges from 1 to the total number of fiber cross-sections in the target image. Using the magnitude of the out-of-plane angle of fiber i on the reference image, $|\theta_i^r|$, and the in-plane angle of fiber i on the reference image, $|\theta_i^r|$, the two candidate positions for the centroid of fiber i on the target image were computed by

$$x_j^c = x_i^r + \frac{h}{\tan(90 - \theta_j^r)} \cos\phi_i^r$$

$$y_j^c = y_i^r - \frac{h}{\tan(90 - \theta_j^r)} \sin\phi_i^r$$
(3)

where j ranges from 1 to 2 and θ_i^r is given by

$$\theta_j^r = \begin{cases} +|\theta_i^r|, & j=1\\ -|\theta_i^r|, & j=2 \end{cases} \tag{4}$$

It is important to note that the origin of an image in MATLAB is the top left corner of the image, resulting in a positive y direction that points vertically down.

The two candidate centroid positions (one for $+|\theta_i^r|$ and one for $-|\theta_i^r|$) were simultaneously compared with the fiber centroids on the fiber target image, as shown in Fig. 4D. A target fiber cross-section was considered for matching if its centroidal position satisfied the following criteria:

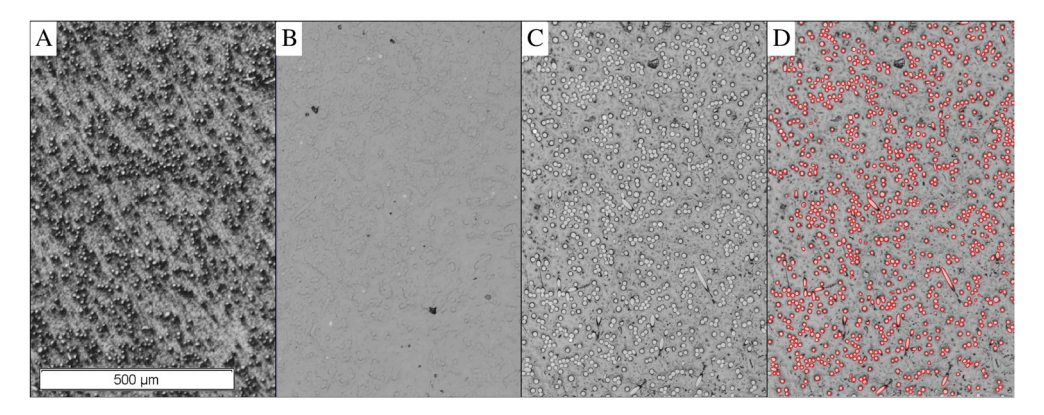


Fig. 3. Progression of the surface after (A) rough polishing, (B) final polishing, (C) plasma etching, and (D) post-processing with elliptical fits around the cross-section of each fiber.

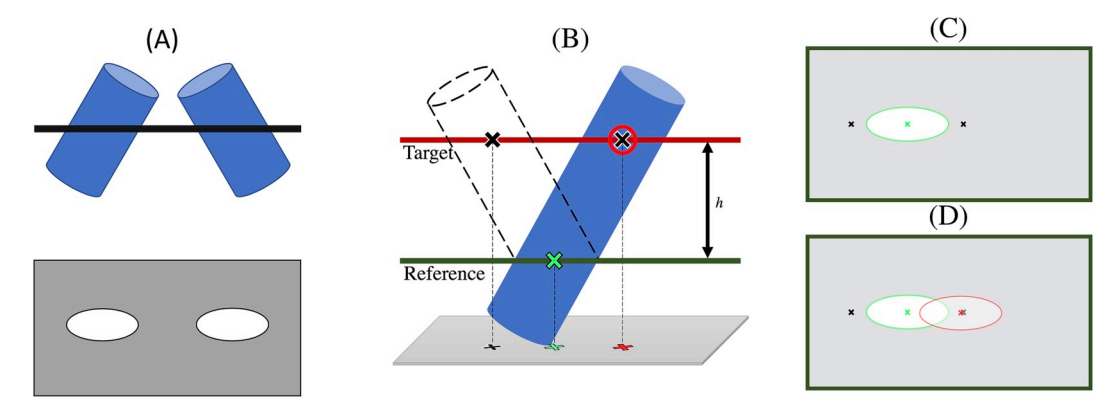


Fig. 4. Schematic showing (A) the ambiguity of the out-of-plane angle θ , (B) successive polishing to determine the sign of θ , (C) the reference image with the two predicted centroid positions, and (D) the reference image and target image schematically overlaid to determine the sign of θ .

$$\sqrt{(x_i^c - x_k^t)^2 + (y_i^c - y_k^t)^2} < \frac{d}{2}$$
 (5)

where d/2 is the fiber radius (in this case, approximately 9 pixels is used, corresponding to 5.86 μ m). If only one target fiber matched and $|\theta_i^r-\theta_k^t|\leq 15^\circ$, it was considered a matching fiber. If more than one target fiber matched with the candidate positions (which can occur for groups of very closely packed fibers), the closely packed target fibers were organized in order of $minimum(|\phi_i^r-\phi_k^t|)$. The target fiber with the minimum difference in ϕ which also satisfied $|\theta_i^r-\theta_k^t|\leq 15^\circ$ was considered the final matching fiber. Based on whether $+|\theta_i^r|$ or $-|\theta_i^r|$ yielded the match from the reference fiber to the target fiber, the sign of θ_i^r was determined and the A_{13} and A_{23} components for each fiber were computed as can be seen in Fig. 5, where the arrows in Fig. 5A point from the reference centroid position (x_i^r, y_i^r) to the matched target fiber centroid position (x_k^r, y_k^t) . An outline of the algorithm is also provided in the Appendix.

2.4.3. Destructively measuring the fiber length distribution

In order to destructively quantify the fiber length distribution, a second specimen was selected because the first specimen was sectioned and polished thereby inherently cutting through the fibers, rendering the specimen unusable for a fiber length comparison. The second specimen was placed inside a fitted aluminum cage, and was heated to

538 °C and held at temperature for 1 h to decompose the polymer matrix, leaving behind a tangled web of glass fibers (commonly referred to as a matrix 'burn-off'). This web of glass fibers was down selected using an epoxy cylinder with an approximate diameter of 3.6 mm that was injected using a syringe into the web of glass fibers. The down selection was then extracted and heated to 538 °C and held at temperature for 1 h to decompose the epoxy, leaving behind the down selected fibers [40]. Next, the fibers were suspended in distilled water and were sonicated to induce fiber separation. The water containing the glass fibers was poured into a petri dish and was heated to evaporate the water. Finally, the petri dish containing the separated fibers was imaged in an Olympus BX51M reflected light microscope equipped with an X-Y-Z stage to enable acquisition of many high resolution images and automated stitching to characterize a large region. This invasive technique has inherent challenges, including - but not limited to - potential damage induced to fibers during the matrix 'burn-off' and sonication processes, and difficulty in the detection of very short fibers in a suspension [3,20].

3. Results

3.1. Fiber and porosity volume fractions

Fiber volume fraction, as determined from X-ray μ -CT, was compared to the fiber area fraction, determined by the optically acquired reference

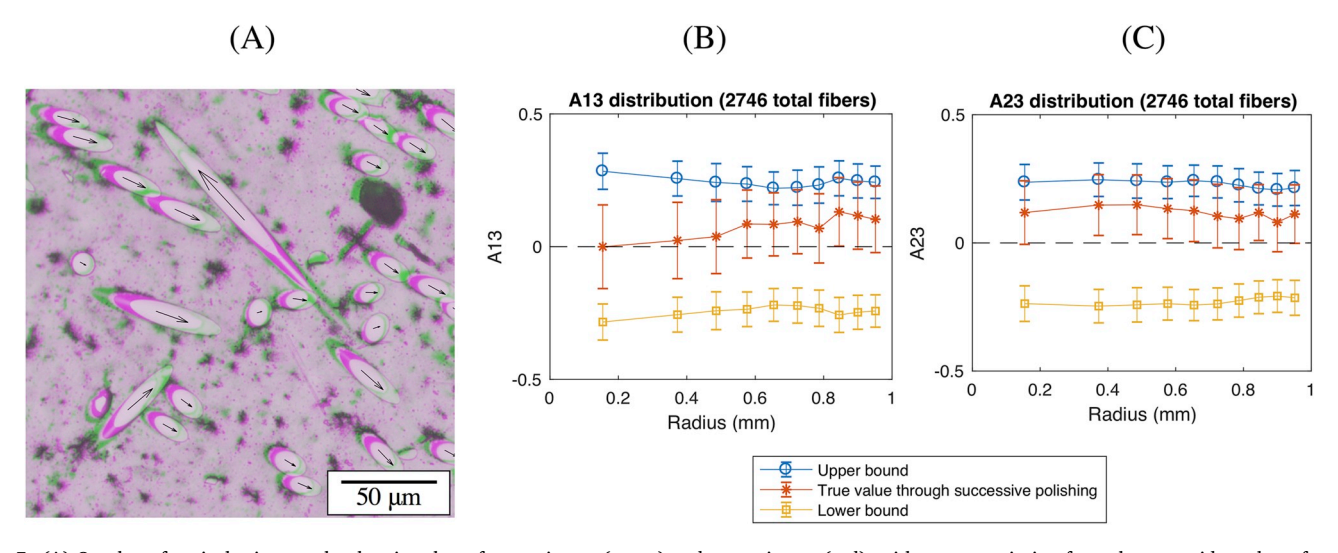


Fig. 5. (A) Overlay of optical micrographs showing the reference image (green) and target image (red), with arrows pointing from the centroid on the reference image to the centroid on the target image, as well as plots of the (B) A_{13} and the (C) A_{23} components of the A_{ij} tensor, showing the upper bound, the lower bound, and the true value determined through successive polishing and automatic image analysis. (For interpretation of the references to colour in this figure legend, the reader is referred to the Web version of this article.)

image, at the location of the fiducial marker adhered to the center of the specimen's gauge section. It was found that the fiber volume fraction determined through non-destructive X-ray μ -CT of the gauge section was 13.4%, while the fiber area fraction determined with destructive optical microscopy was 13.3%. The porosity volume fraction non-destructively was found to be 2.6%, while the porosity area fraction determined from destructive optical microscopy at the matching region was found to be 2.3%.

3.2. Fiber orientation distribution

The fiber orientations using X-ray μ -CT and then optical microscopy for the exact same region of interest (determined using the aluminum fiducial marker on the same specimen) was computed. This allowed for a one-to-one comparison of the same fibers sampled in the X-ray μ -CT images and the destructive optical image. Using 10 concentric annuli with equal areas spanning the specimen's radius, each component of the A_{ij} tensor was averaged along the radial direction of the specimen and is plotted in Fig. 6, with error bars representing plus and minus one standard deviation. Additionally, the generalized Herman's 3D orientation factor [35,41], which provides a general alignment criteria (whereas f=0 for totally random alignment, f=0.5 for moderate alignment, and f=1 for complete alignment) was computed by

$$f = \frac{3}{2} A_{ij} A_{ji} - \frac{1}{2} \tag{6}$$

and non-destructively determined to be 0.52 and destructively determined to be 0.46.

Furthermore, the mean fiber alignments $\overline{\Phi}_X$, $\overline{\Phi}_Y$, and $\overline{\Phi}_Z$ with respect to the X, Y, and Z axes (respectively) can be found in Table 1 and were computed by

$$\overline{\Phi}_{X} = \cos^{-1} \left(\begin{bmatrix} 1 & 0 & 0 \\ 0 & 0 & 0 \\ 0 & 0 & 0 \end{bmatrix} : \overline{A}_{ij} \right)$$
 (7)

 Table 1

 Microstructural parameters computed using both techniques.

Parameter	Non-Destructive Analysis	Destructive Analysis
Fiber Volume Fraction	13.4%	13.3%
Porosity Volume Fraction	2.6%	2.3%
Number Average Fiber Length	196.1 μm	209.9 μm
Weight Average Fiber Length	278.8 μm	305.3 μm
Average Fiber Alignment with X	87.7°	82.3°
Average Fiber Alignment with Y	81.5°	83.3°
Average Fiber Alignment with Z	35.6°	41.5°
3D Fiber Orientation Factor	0.52	0.46
Young's Modulus along X, E_{11}	3.07 GPa	2.93 GPa
Young's Modulus along Y, E_{22}	3.01 GPa	2.87 GPa
Young's Modulus along Z, E_{33}	4.62 GPa	5.60 GPa
Poisson's Ratio in the X–Y, ν_{12}	0.44	0.50
Poisson's Ratio in the Y-Z, ν_{23}	0.26	0.24
Poisson's Ratio in the X-Z, ν_{13}	0.41	0.33

$$\overline{\Phi}_{Y} = \cos^{-1} \left(\begin{bmatrix} 0 & 0 & 0 \\ 0 & 1 & 0 \\ 0 & 0 & 0 \end{bmatrix} : \overline{A}_{ij} \right)$$
 (8)

$$\overline{\Phi}_Z = \cos^{-1} \left(\begin{bmatrix} 0 & 0 & 0 \\ 0 & 0 & 0 \\ 0 & 0 & 1 \end{bmatrix} : \overline{A}_{ij} \right)$$
 (9)

3.3. Fiber length distribution

The fiber length distribution was non-destructively determined from the X-ray μ -CT images by using an in-house MATLAB algorithm to compute the distance between the end points of each fiber which were extracted using the post-processing algorithms described in Ref. [31]. Destructively, the fiber lengths were measured manually from the optically acquired images of fibers after matrix decomposition using the

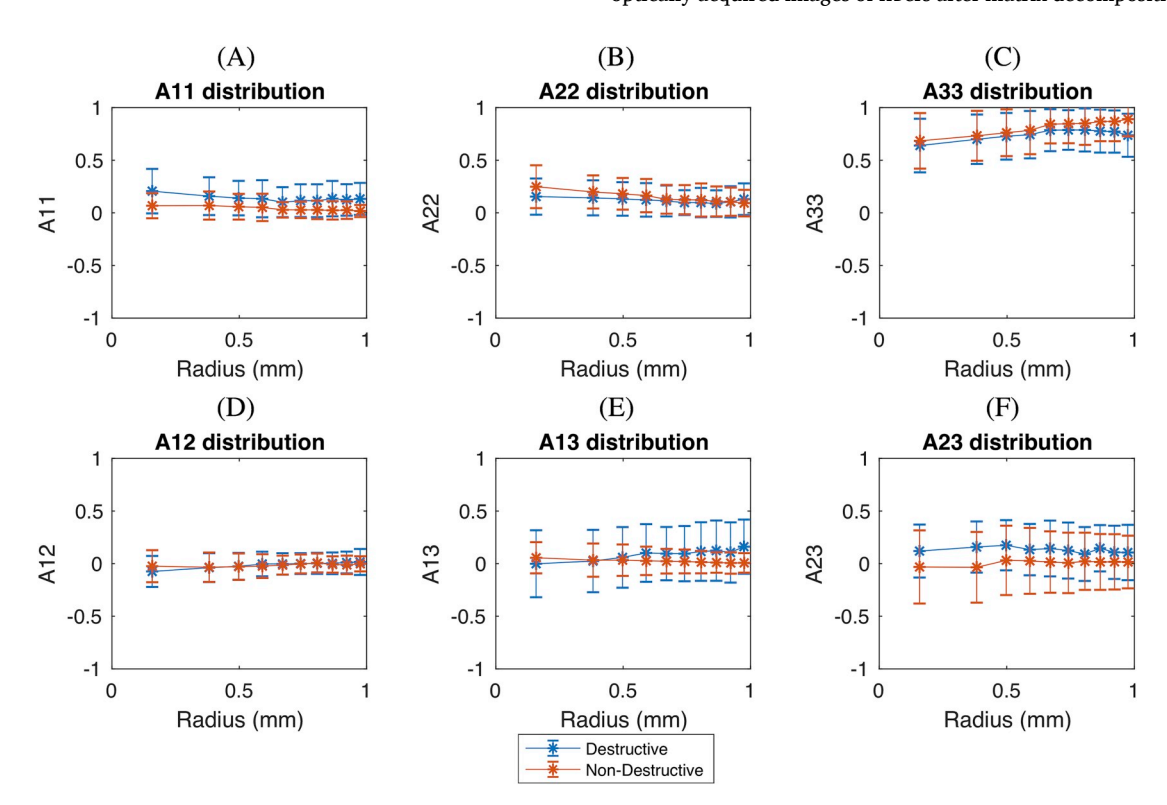


Fig. 6. The radial fiber orientation distribution averaged along equal area concentric annuli of the specimen for (A) A_{11} , (B) A_{22} , (C) A_{33} , (D) A_{12} , (E) A_{13} , and (F) A_{23} from both non-destructive and destructive characterization of the same fibers.

manual measurement tools in OLYMPUS stream. The weight based fiber length distributions were computed [20,21] by

$$w_i = \frac{N_i L_i}{\sum_k N_k L_k} \tag{10}$$

and are provided in Fig. 8, where automatic detection using the non-destructive technique captured 58,082 fibers and manual measurement of fibers using the destructive technique captured 2,151 fibers. Since particles and small fragments of fibers are not of interest in this study, only fibers with an aspect ratio greater than 5 were included. Furthermore, the average fiber lengths are provided in Table 1, including the weight average fiber length, which was computed [20,21] by

$$L_{w} = \frac{\sum N_{i}L_{i}^{2}}{\sum N_{i}L_{i}} \tag{11}$$

4. Discussion

In general, it is important to recognize some of the differences in cost and implementation of each destructive and non-destructive technique. Destructive approaches use less expensive equipment: typically a polishing machine, a furnace, and an optical microscope equipped with an X-Y-Z stage, whereas the final optical images can be used to estimate the fiber and porosity volume fractions, and compute the fiber orientation and length distributions. An advantage of destructive approaches is that the magnification of the images can be adjusted depending on the objective lenses used with the microscope. However, the quality of the microscopic image is directly influenced by the skill of the polisher and the contrast between different microstructural features. This contrast may require enhancement with the use of plasma etching, which can be expensive.

On the other hand, X-ray μ -CT is non-contact in nature, thereby allowing a non-destructive analysis of the specimen. However, it requires relatively more expensive X-ray equipment, a small specimen size with some restrictions in geometry (limiting fiber length

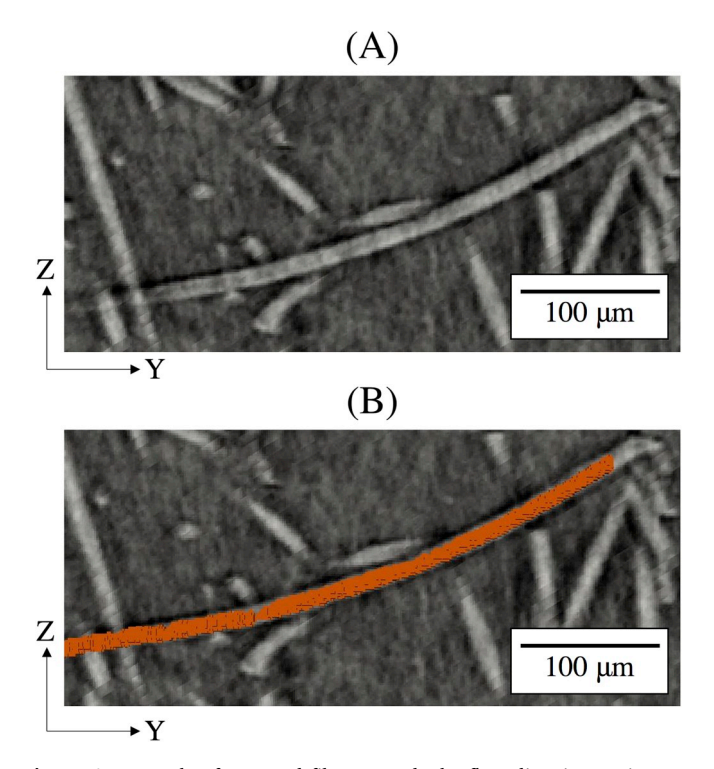


Fig. 7. An example of a curved fiber towards the flow direction, Z, in a tomography image (A) with its detected 3D morphology overlaid in (B).

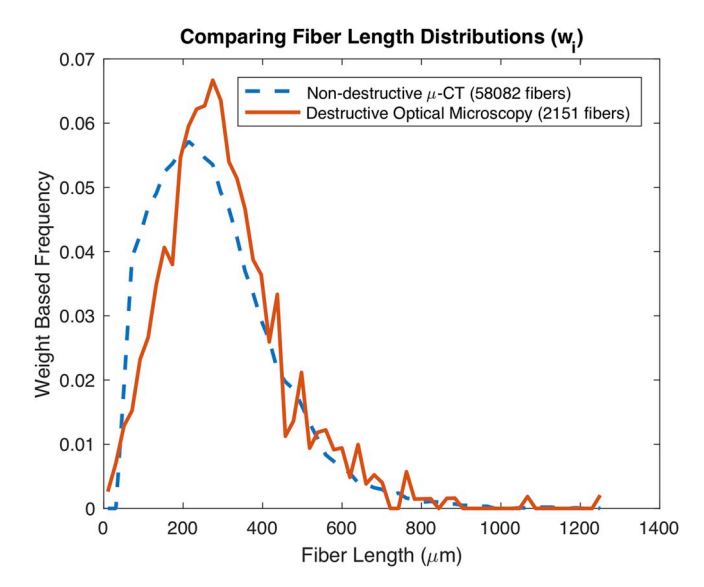


Fig. 8. Comparison of the weight fiber length distributions determined non-destructively and destructively.

measurements), and 360° access to the volume of interest. Non-destructive X-ray μ -CT is capable of resolving almost all details of the microstructure presented in the 3D image from the same specimen, including the morphology of the porosity (yielding porosity volume fraction) and the morphology of the fibers (yielding fiber volume fraction, fiber orientation, and fiber length distributions) which is advantageous compared to destructive methods, which require separate specimens for the fiber orientation and fiber length measurements. The biggest disadvantage is the rigorous, computationally expensive, and sensitive post-processing that must be conducted to extract meaningful information from the images which inherently include fluctuations in intensity due to fluctuations in X-ray energy. However, once successfully post-processed and reconstructed in 3D [31], the quantity and quality of the information gathered is comprehensive and robust.

When investigating the microstructural attributes of the composite, it was found that the fiber volume fraction determined through nondestructive X-ray μ -CT (13.4%) matched closely to the destructive optical microscopy's fiber area fraction (13.3%) which also matched closely to what was expected from the manufacturing specifications (13.7%). Therefore, fiber volume fraction can be expected to match well using both techniques. The porosity volume fraction determined through X-ray μ -CT (2.6%) was slightly higher than that which was computed through porosity area fraction from the destructive optical microscopy images (2.3%). This can be attributed to very small pores which were captured in the X-ray μ-CT images but were not captured in the destructive optical images, as can be seen in Fig. 9. To further quantify this, a one-to-one porosity comparison between the X-ray μ -CT images and the optical microscopy image was conducted, and it was found that pores smaller than approximately 700 µm³ (equivalent to spherical pores with radii less than ~5.5 μm) were not captured by sectioning and polishing, because they were likely filled in with polished polymer during the polishing routine (sometimes referred to as matrix smearing). After extracting only pores with a volume greater than 700 μm³, the porosity volume fraction computed non-destructively was 2.3%, matching exactly to the porosity area fraction computed destructively.

The fiber orientation distribution matched relatively well between both methods as was seen in Fig. 6 for all of the components of the A_{ij} tensor, with the non-destructive method reporting a slightly better alignment as can be seen in Table 1. Small deviations between the orientation distribution data are due to a combination of small perturbations in the elliptical fitting of the pixelized elliptical cross-sections of

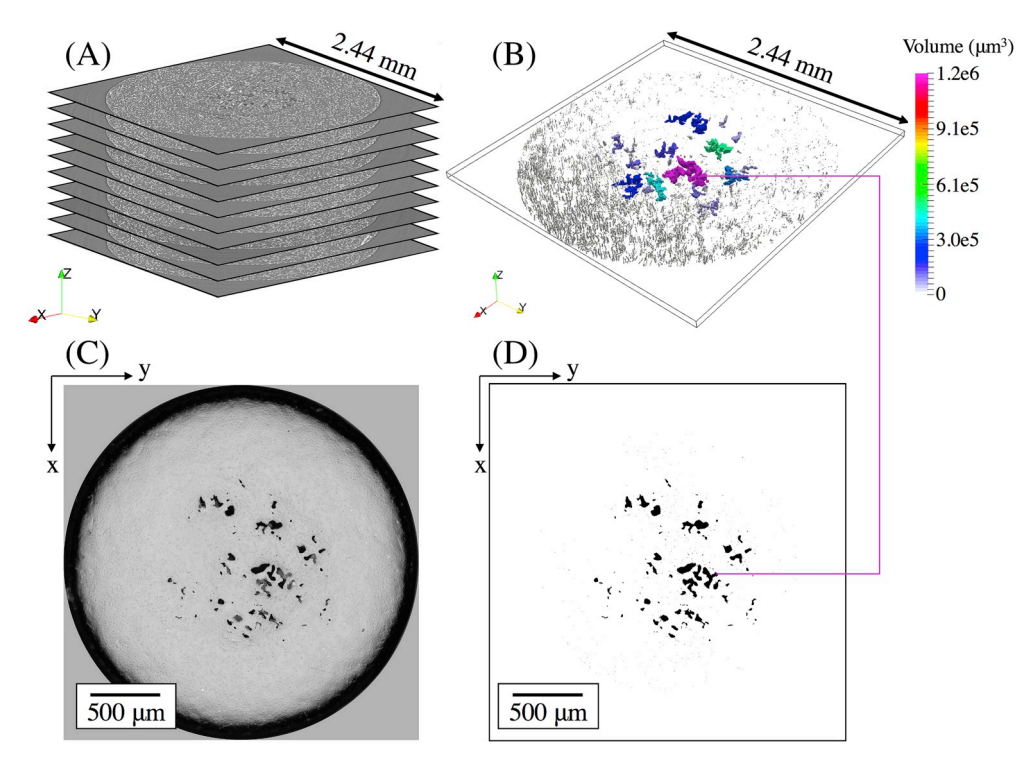


Fig. 9. A sample of the of X-ray μ -CT images (A) which included the matching optical microscopy image plus and minus 26 μ m, the detected 3D porosity (B), the surface of the specimen achieved through polishing but before plasma etching of the matching region (C) as well as the 2D porosity detected from the optical micrograph (D).

fibers, which can impact the average values creating fluctuations in the average A_{ij} components in the range of 0.05-0.09 [16], as well as the fact the X-ray μ -CT is inherently 3D and therefore captures the full length of each fiber, which includes gentle curvatures of fibers towards the flow direction [42,43] as can be seen in Fig. 7, thereby reporting a slightly better alignment. In general, average fiber alignment with respect to each unit vector of the Cartesian coordinate axes can be expected to differ by less than 6° using both techniques.

The fiber length distributions for both the destructive and nondestructive techniques, which were shown in Fig. 8, matched relatively well exhibiting a small difference in the distributions and their corresponding average values provided in Table 1. This is due to two compounding factors, one being that in the destructive analysis it is difficult to manually find all the small fibers which can be mistaken for noise, and the second being that in the non-destructive analysis, natural fluctuations in intensity due to the X-ray scattering and tomographic reconstruction can sometimes result in a reduction of intensity along the length of a fiber, causing some fibers to appear to have a discontinuity. Furthermore, X-ray μ-CT images of the volume have a limited height (in this work, 1.6 mm and therefore on the order of the maximum fiber length) introducing a bias in the length distributions since some fibers touch the upper and lower boundaries of the images. Despite this discrepancy, the maximum fiber length was very similar as was seen in Fig. 8, and the difference in the number average fiber length was 13.8 μm (corresponding to a difference in average aspect ratio of 1.38), which is relatively small and therefore would not have a notable effect on mechanical stiffness predictions [16]. Using the microstructural properties detected using both techniques, stiffness values in each direction were computed [16,18,44] and can be found in Table 1. It can be seen that stiffness values are close, but discrepancies exist, specifically in E_{33} aligned in the flow direction, mainly due to the slightly higher alignment detected non-destructively, which was on average 6° more aligned with the flow direction. These discrepancies in the overall stiffness properties of the composite illustrate the importance and need for precise microstructure characterization techniques.

5. Conclusion

This work focused on methods used to characterize fiber and porosity volume fraction, fiber orientation, and fiber length distributions in short fiber reinforced composites. Non-destructive X-ray μ -CT images were segmented to extract gas-phase porosity, and then rigorously post-processed to detect each 3D fiber using a supervised iterative algorithm [31]. The same specimen was then analyzed at a matching region using successive polishing, plasma etching, and optical imaging to conduct a one-to-one comparison of the porosity volume fraction, fiber volume fraction, and fiber orientation distributions, utilizing an algorithm that was created to automatically resolve the ambiguous A_{13} and A_{23} components of the A_{ij} fiber orientation tensor. A second specimen machined from the same rod was selected for matrix 'burn-off' in a furnace, down-selection, secondary 'burn-off,' suspension of fibers in water, sonication, evaporation, and optical imaging to compare the fiber length distributions. Below are the significant findings from this study:

- The fiber volume fraction computations matched very well using both techniques.
- 2. The porosity volume fraction detected by sectioning and polishing was slightly lower than that detected in the X-ray $\mu\text{-CT}$ images due to pores smaller than 700 μm^3 (equivalent to spherical pores with radii less than ~5.5 μm) being filled in with polymer during polishing. When considering only pores greater than 700 μm^3 , the volume fraction computations matched almost exactly.
- 3. The A_{ij} fiber orientation distribution determined non-destructively and destructively matched fairly well (differing no more than 6° on average with respect to each Cartesian coordinate axes) with the non-destructive approach reporting a slightly higher alignment due to its ability to capture curvatures of 3D fibers in the injection molding flow direction.
- 4. The average fiber length when computed non-destructively and destructively matched within 13.8 μm, with the non-destructive approach reporting a slightly lower average length due to inherent

fluctuations in intensity of the X-ray μ -CT images and limitations in the X-ray μ -CT scanning volume, and with the destructive approach reporting a slightly higher average length due to difficulty in manually finding and measuring every short fiber.

Overall, the effects of destructive and non-destructive techniques and their ability to detect microstructural features were studied for the same exact region of interest. This analysis provides information necessary for engineers and researchers to identify the advantages/disadvantages of both approaches and understand the quantitative differences in microstructural characterization when using each method in

by the US Department of Energy, Office of Science, and Office of Basic Energy Sciences under Contract No. DE-AC02 06CH11357.

Appendix A. Supplementary data

Supplementary data to this article can be found online at https://doi.org/10.1016/j.compscitech.2019.107843.

Appendix

- 1. **READ** reference '.csv' ellipse fit file containing $x^r, y^r, |\theta^r|, \phi^r$
- 2. **READ** target '.csv' ellipse file containing x^t , y^t , $|\theta^t|$, ϕ^t
- 3. **READ** optical microscopy images
- 4. **SET** specimen radius and center coordinates
- 5. **SET** height between reference and target images, h = 7 (7 pixels corresponding to ~4.5 μm)
- 6. **SET** search limit criteria, limit = 9 (9 pixels corresponding to ~5.8 μm , approximately half the fiber diameter)
- 7. GET all centroidal parameters from the reference and target files

Search and Match Procedure

FOR reference fiber = 1 : length(reference fibers)

- a. CALCULATE projected translational displacement on the target image
- c. CALCULATE the candidate positions x_i^c and y_i^c

FOR *target fiber* = 1 : length(*target fibers*)

- a. CALCULATE the distance between the 2 candidate positions and the target fiber
 b. SELECT target fiber if it matches limit criteria
- c. CALCULATE number of matches based on limit criteria
- d. SET best match based on the minimum difference of the in-plane-angle (if more than one match present)
- e. SET best match if the difference in θ is less than 15° (which is selected as a suitable threshold for comparison)
- f. **SET** sign of θ_i^r based on the candidate that yielded the match

END

Save and Visualize

- 8. **SAVE** updated fiber properties with sign of θ included as a '.csv'
- 9. **SHOW** optical microscopy images overlaid using *imfuse* with arrows using *quiver*

Algorithm 1. Reference and Target Fiber Matching

order to confidently qualify composite materials and predict their mechanical behavior.

Declaration of competing interest

The authors declare that they have no known competing financial interests or personal relationships that could have appeared to influence the work reported in this paper.

Acknowledgements

The authors gratefully acknowledge support from the National Science Foundation CMMI MoM, Award No.1662554, and DARPA, Award No. HR0011-17-2-0069. The authors would like to thank Dr. Bhisham Sharma, currently at Wichita State University, for developing the initial 2D characterization algorithms and Dr. Alan Wedgewood of Dupont for providing the material. The use of the Advance Photon Source is granted

References

- K. Ramani, D. Bank, N. Kraemer, Effect of screw design on fiber damage in extrusion compounding and composite properties, Polym. Compos. 16 (1995) 258–266, https://doi.org/10.1002/pc.750160310.
- [2] R. Bailey, H. Kraft, A study of fibre attrition in the processing of long fibre reinforced thermoplastics, Int. Polym. Process. 2 (1987) 94–101.
- [3] K. Stade, Techniques for compounding glass fiber-reinforced thermoplastics, Polym. Eng. Sci. 17 (1977) 50–57, https://doi.org/10.1002/pen.760170110.
- [4] D. Wall, Co-rotating twin screw extruders, Polym. Compos. 70 (1989).
- [5] J.L. Kardos, J.C. Halpin, Short predicting the strength and toughness of fiber composites, Macromol. Symp. 153 (1999) 139–153, https://doi.org/10.1002/ masv.19991470114.
- [6] R. Byron Pipes, R.L. McCullough, D.G. Taggart, Behavior of discontinuous fiber composites: fiber orientation, Polym. Compos. 3 (1982) 34–39, https://doi.org/ 10.1002/pc.750030107.
- [7] M. Gupta, K.K. Wang, Fiber orientation and mechanical properties of short-fiber-reinforced injection-molded composites: simulated and experimental results, Polym. Compos. 14 (1993) 367–382, https://doi.org/10.1002/pc.750140503.

- [8] A. Vaxman, M. Narkis, A. Siegmann, S. Kenig, Short-Fiber-Reinforced Thermoplasitcs. Part III: Effect of Fiber Length on Rheological Properties and Fiber Orientation, vol. 10, 1989.
- [9] S.Y. Fu, B. Lauke, Effects of fiber length and fiber orientation distributions on the tensile strength of short-fiber-reinforced polymers, Compos. Sci. Technol. 56 (1996) 1179–1190, https://doi.org/10.1016/S0266-3538(96)00072-3.
- [10] M.P. Connolly, The measurement of porosity in composite materials using infrared thermography, J. Reinf. Plast. Compos. 11 (1992) 1367–1375.
- [11] S.H. McGee, R.L. McCullough, Characterization of fiber orientation in short-fiber composites, J. Appl. Phys. 55 (1984) 1394–1403, https://doi.org/10.1063/ 1.33230
- [12] G.M. Vélez-García, P. Wapperom, D.G. Baird, A.O. Aning, V. Kunc, Unambiguous orientation in short fiber composites over small sampling area in a center-gated disk, Compos. Part A Appl. Sci. Manuf. 43 (2012) 104–113, https://doi.org/ 10.1016/i.compositesa.2011.09.024.
- [13] B. Mlekusch, Thermoelastic properties of short-fibre-reinforced thermoplastics, Compos. Sci. Technol. 59 (1999) 911–923, https://doi.org/10.1016/S0266-3538 (98)00133-X.
- [14] L. Avérous, J.C. Quantin, D. Lafon, A. Crespy, Determination of 3D fiber orientations in reinforced thermoplastics, using scanning electron microscopy, Acta Stereol. (1995).
- [15] R.S. Bay, C.L. Tucker, Stereological measurement and error estimates for threedimensional fiber orientation, Polym. Eng. Sci. 32 (1992) 240–253, https://doi. org/10.1002/pen.760320404.
- [16] B.N. Sharma, D. Naragani, B.N. Nguyen, C.L. Tucker, M.D. Sangid, Uncertainty quantification of fiber orientation distribution measurements for long-fiberreinforced thermoplastic composites, J. Compos. Mater. (2017), 002199831773353, https://doi.org/10.1177/0021998317733533.
- [17] U. Yilmazer, M. Cansever, Effects of processing conditions on the fiber length distribution and mechanical properties of glass fiber reinforced nylon-6, Polym. Compos 23 (2002) 61–71, https://doi.org/10.1002/pc.10412.
- [18] B.N. Nguyen, S.K. Bapanapalli, J.D. Holbery, M.T. Smith, V. Kunc, B.J. Frame, J. H. Phelps, C.L. Tucker, Fiber length and orientation in long-fiber injection-molded thermoplastics Part I: modeling of microstructure and elastic properties, J. Compos. Mater. 42 (2008) 1003–1029, https://doi.org/10.1177/002198308088606.
- [19] S.Y. Fu, B. Lauke, E. M\u00e4der, C.Y. Yue, X. Hu, Tensile properties of short-glass-fiberand short-carbon-fiber-reinforced polypropylene composites, Compos. Part A Appl. Sci. Manuf. 31 (2000) 1117–1125, https://doi.org/10.1016/S1359-835X(00) 00068-3.
- [20] B.N. Sharma, S.A. Kijewski, L.S. Fifield, Y. Shin, C.L. Tucker, M.D. Sangid, Reliability in the characterization of fiber length distributions of injection molded long carbon fiber composites, Polym. Compos. 39 (2018) 4594–4604, https://doi. org/10.1002/pc.24571.
- [21] J.H. Phelps, A.I. Abd El-Rahman, V. Kunc, C.L. Tucker, A model for fiber length attrition in injection-molded long-fiber composites, Compos. Part A Appl. Sci. Manuf. 51 (2013) 11–21, https://doi.org/10.1016/j.compositesa.2013.04.002.
- [22] M. Kawamura, S. Ikeda, S. Morita, Y. Sanomura, Unambiguous determination of 3D fiber orientation distribution in thermoplastic composites using SAM image of elliptical mark and interference fringe, J. Compos. Mater. 39 (2005) 287–299, https://doi.org/10.1177/0021998305046463.
- [23] Y. Lee, S. Lee, J. Youn, K. Chung, T. Kang, Characterization of fiber orientation in short fiber reinforced composites with an image processing technique, Mater. Res. Innov. 6 (2002) 65–72, https://doi.org/10.1007/s10019-002-0180-8.
- [24] N.C. Davidson, A.R. Clarke, G. Archenhold, Large-area, high-resolution image analysis of composite materials, J. Microsc. 185 (1997) 233–242, https://doi.org/ 10.1046/j.1365-2818.1997.1560712.x.
- [25] J. Lux, C. Delisée, X. Thibault, 3D characterization of wood based fibrous materials: an application, Image Anal. Stereol. 25 (2011) 25, https://doi.org/10.5566/ias. v25.025.35
- [26] M. Tausif, B. Duffy, S. Grishanov, H. Carr, S.J. Russell, Three-dimensional fiber segment orientation distribution using X-ray microtomography, Microsc. Microanal. 20 (2014) 1294–1303, https://doi.org/10.1017/S1431927614000695.

- [27] H. Altendorf, D. Jeulin, 3D directional mathematical morphology for analysis of fiber orientations, Image Anal. Stereol. 28 (2009) 143–153, https://doi.org/ 10.5566/ias.v28.p143-153.
- [28] F. Malmberg, J. Lindblad, C. Östlund, K.M. Almgren, E.K. Gamstedt, Measurement of fibre-fibre contact in three-dimensional images of fibrous materials obtained from X-ray synchrotron microtomography, Nucl. Instrum. Methods Phys. Res. Sect. A Accel. Spectrom. Detect. Assoc. Equip. 637 (2011) 143–148, https://doi.org/ 10.1016/j.nima.2011.01.080.
- [29] H. Shen, S. Nutt, D. Hull, Direct observation and measurement of fiber architecture in short fiber-polymer composite foam through micro-CT imaging, Compos. Sci. Technol. 64 (2004) 2113–2120, https://doi.org/10.1016/j. compscitech.2004.03.003.
- [30] E.N. Landis, D.T. Keane, X-ray microtomography, Mater. Char. 61 (2010) 1305–1316, https://doi.org/10.1016/j.matchar.2010.09.012.
- [31] R.F. Agyei, M.D. Sangid, A supervised iterative approach to 3D microstructure reconstruction from acquired tomographic data of heterogeneous fibrous systems, Compos. Struct. 206 (2018) 234–246, https://doi.org/10.1016/j. compstruct.2018.08.029.
- [32] S.C. Garcea, Y. Wang, P.J. Withers, X-ray computed tomography of polymer composites, Compos. Sci. Technol. 156 (2018) 305–319, https://doi.org/10.1016/ j.compscitech.2017.10.023.
- [33] M.J. Emerson, Y. Wang, P.J. Withers, K. Conradsen, A.B. Dahl, V.A. Dahl, Quantifying fibre reorientation during axial compression of a composite through time-lapse X-ray imaging and individual fibre tracking, Compos. Sci. Technol. 168 (2018) 47–54, https://doi.org/10.1016/j.compscitech.2018.08.028.
- [34] A. Bernasconi, F. Cosmi, P.J. Hine, Analysis of fibre orientation distribution in short fibre reinforced polymers: a comparison between optical and tomographic methods, Compos. Sci. Technol. 72 (2012) 2002–2008, https://doi.org/10.1016/j. compscitech.2012.08.018.
- [35] S. Advani, C.L. Tucker III, The use of tensors to describe and predict fiber orientation in short fiber composites, J. Rheol. (N. Y. N. Y). 31 (1987) 751–784, https://doi.org/10.1122/1.549945.
- [36] P.J. Hine, N. Davidson, R.A. Duckett, A.R. Clarke, I.M. Ward, Hydrostatically extruded glass-fiber-reinforced polyoxymethylene. I: the development of fiber and matrix orientation, Polym. Compos. 17 (1996) 720–729, https://doi.org/10.1002/ pc.10664.
- [37] B. Mlekusch, Fibre orientation in short-fibre-reinforced thermoplastics II. Quantitative measurements by image analysis, Compos. Sci. Technol. 59 (1999) 547–560.
- [38] D. Gürsoy, F. De Carlo, X. Xiao, C. Jacobsen, TomoPy: a framework for the analysis of synchrotron tomographic data, J. Synchrotron Radiat. 21 (2014) 1188–1193, https://doi.org/10.1107/S1600577514013939.
- [39] I. Arganda-Carreras, V. Kaynig, C. Rueden, K.W. Eliceiri, J. Schindelin, A. Cardona, H.S. Seung, Trainable Weka Segmentation: a machine learning tool for microscopy pixel classification, Bioinformatics 33 (2017) 2424–2426, https://doi.org/ 10.1093/bioinformatics/btx180.
- [40] V. Kunc, B. Frame, J. Pryor, B.N. Nguyen, C.L. Tucker III, S. Case, D. Penumadu, E. W. Guffey, Techniques and results for fiber length distribution determination as a function of thickness in long fiber reinforced injection molded thermoplastics, Oak Ridge Natl. Lab. Rep. (2008).
- [41] P.H. Hermans, Contribution to the Physics of Cellulose Fibres, Elseview Publishing Company, Iinc., London, 1946.
- [42] C.G. Joung, N. Phan-Thien, X.J. Fan, Viscosity of curved fibers in suspension, J. Nonnewton. Fluid Mech. 102 (2002) 1–17, https://doi.org/10.1016/S0377-0257(01)00163-X.
- [43] S. Bapanapalli, B.N. Nguyen, Prediction of elastic properties for curved fiber polymer composites, Polym. Compos. (2008), 10.1002.
- [44] C.L. Tucker, E. Liang, Stiffness predictions for unidirectional short-fiber composites, Compos. Sci. Technol. 59 (1999), https://doi.org/10.1016/S0266-3538(98)00120-1.